



# Obtaining and Characterization of Super-Hydrophobic Nickel Coatings Applied on ASTM A36 Carbon Steel Via Electrodeposition as an Alternative for Anticorrosive Protection

Walter Leandro Cordeiro da Silva Filho<sup>a\*</sup> , Giuliana Taissa Farias Salgueiro<sup>a</sup>,

Maria Isabel Collasius Malta<sup>a</sup> , Jedaias Januário da Silva<sup>a</sup> , Rafael Gleymir Casanova da Silva<sup>b</sup> ,

Severino Leopoldino Urtiga Filho<sup>a</sup>, Magda Rosângela Santos Vieira<sup>a</sup> 

<sup>a</sup>Universidade Federal de Pernambuco, Departamento de Engenharia Mecânica, Avenida Professor Moraes Rego, 1235, Cidade Universitária, 50670-901, Recife, PE, Brasil.

<sup>b</sup>Universidade Federal de Pernambuco, Departamento de Engenharia Química, Avenida Professor Moraes Rego, 1235, Cidade Universitária, 50670-901, Recife, PE, Brasil.

Received: February 09, 2024; Revised: April 13, 2024; Accepted: May 20, 2024

The present study aimed to develop and characterize super-hydrophobic nickel coatings through the electrodeposition process, employing myristic acid as a surface energy reducing agent, with the objective of enhancing corrosion resistance. ASTM A36 carbon steel (E00) specimens served as substrates for the application of three different coating conditions: pure nickel (E10); nickel associated with myristic acid (E01); and a bilayer structure consisting of a base layer of pure nickel succeeded by an additional layer of nickel enriched with myristic acid (E11). The samples were characterized through Optical Microscopy (OM), Scanning Electron Microscopy (SEM), Energy Dispersive Spectroscopy (EDS), X-ray Diffraction (XRD), and Fourier Transform Infrared Spectroscopy (FTIR). Corrosion resistance of the coatings was analyzed through potentiodynamic polarization (PP) tests and electrochemical impedance spectroscopy (EIS). XRD and FTIR tests confirmed the deposition of metallic nickel onto the substrate and the successful incorporation of the surface energy reducing agent. Micrographs illustrated the distinctive cauliflower-like clusters in the E11 coating, denoting its pronounced super-hydrophobic characteristics, culminating in a contact angle of 165°. Corrosion tests demonstrated superior anticorrosive behavior in the E11 sample, as evidenced by a heightened corrosion potential, diminished anodic current density, and an augmented impedance modulus. The results emphasize the role of superhydrophobicity in influencing the corrosion resistance of the developed coatings.

**Keywords:** Nickel Coating, Electrodeposition, Super-hydrophobicity, Corrosion Resistance, ASTM A36 Carbon Steel.

## 1. Introduction

The phenomenon of super-hydrophobicity has been the subject of curiosity and interest among various researchers since the 1970s, when the peculiar wettability behavior of the lotus flower was observed and scientifically described. The lotus flower exhibits high water repellency, imparting the leaves with self-cleaning characteristics that keep the plant free from impurities<sup>1-4</sup>.

This behavior can be observed not only in plants, but also in other natural systems; like the wings and legs of certain insects<sup>2</sup>. Various fly species, such as mayflies, dragonflies, butterflies, and moths present hydrophobic wings, which exhibit enhanced flight capabilities due to the self-cleaning effect conferred by high water repellency<sup>5</sup>. The water strider insect, another noteworthy example, effortlessly walks on water facilitated by the stored air in the micro-nano-roughness on the surface of its legs<sup>6</sup>.

These instances of super-hydrophobicity in nature have become the focus of research, aiming to inspire the

development of artificial surfaces with diverse engineering applications through biomimicry<sup>2-4</sup>. Those studies indicate that the presence of micro-nanostructured roughness combined with a material of low surface energy are the primary factors conferring super-hydrophobic behavior to a surface<sup>7-10</sup>. Characterized by a water contact angle exceeding 150° and a sliding angle below 10°<sup>11-13</sup> super-hydrophobic surfaces (SHS) may possess, in addition to self-cleaning, characteristics such as corrosion resistance, antibacterial properties, antifreeze capability, anti-fouling, and drag reduction<sup>1,14,15</sup>.

The applications of SHS associated with these properties incorporate various sectors. In the healthcare sector, for instance, there is significant interest in super-hydrophobic surfaces with antimicrobial properties<sup>16-18</sup>. In the solar energy sector, the focus is on the self-cleaning property to enhance the efficiency of electricity generation by mitigating dirt accumulation on panels<sup>3,19</sup>. In the food industry, efforts have been directed towards developing super-hydrophobic food packaging to reduce waste. Liquid and pasty foods, like jams and sauces, often adhere to traditional packaging,

\*e-mail: [walter.leandro@ufpe.br](mailto:walter.leandro@ufpe.br)

**Table 1.** Elemental composition of ASTM A36 steel.

Fe (%)	C (%)	Cu (%)	Mn (%)	P (%)	Si (%)	S (%)
98	0.250	0.200	1.03	0.040	0.028	0.050

preventing complete consumption<sup>20</sup>. Additionally, notable applications are emerging in environmental engineering, with the development of water and oil separation systems to mitigate the impact of leaks in seas and oceans due to the significant affinity of SHS for oily compounds<sup>10,14,21,22</sup>.

Among the properties achievable through the development of SHS, increased corrosion resistance is of great importance<sup>1,9,13,18</sup>. Corrosion affects various sectors and industrial areas, imposing an annual cost estimated at 4% of a developing country's GDP. This degradation process occurs through chemical or electrochemical mechanisms associated with environmental influences<sup>18</sup>.

Electrochemical corrosion, occurring in the presence of water, is linked to the formation of an electrochemical cell. Developing surfaces that prevent or delay aqueous access to the material can reduce, control, and even mitigate corrosion<sup>1,12,19</sup>. Thus, super-hydrophobic surfaces can serve as an efficient alternative against the effects of corrosion, contributing to the reduction of annual expenses on repairs, mitigating social, economic, and environmental impacts.

In this context, techniques and processes have been developed based on observations of natural systems<sup>14,23,24</sup>, enabling the acquisition and fabrication of superhydrophobic surfaces on various substrates using various methods, including lithography<sup>25,26</sup>, electrostatic painting<sup>27-30</sup>, sol-gel<sup>31</sup>, chemical vapor deposition<sup>26,32</sup>, layer-by-layer deposition<sup>33,34</sup>, and electrodeposition<sup>5,6,9,11,12,15,35</sup>.

Electrodeposition is defined as the electrolytic reduction of a specific element dissolved in a cationic form (positive nox), occurring on the surface of a conductive substrate in its metallic form (zero nox). This process takes place under the influence of electrical energy<sup>12,19,35,36</sup>. In this technique, an electrolytic cell is employed, incorporating at least one pair of electrodes and an electrolyte. The electrolyte comprises ionic salts of the metal intended for deposition, also known as the electrolytic bath<sup>10,12,35</sup>. The distinctive advantages of electrodeposition, when compared to alternative methods, lie in its simplicity, cost-effectiveness, ease of parameter control, and absence of restrictions on the shape of the substrate to be coated<sup>1,7</sup>.

In this study, a rapid procedure was developed to obtain superhydrophobic nickel coatings via the electrodeposition process, applied to ASTM-A36 steel. The procedure involved creating micro-nanometric hierarchical structures associated with surface energy reducing agents to achieve superior anticorrosive properties.

## 2. Experimental Procedure

### 2.1. Materials

ASTM A36 steel specimens, measuring 10 mm x 15 mm x 3 mm, were used as substrates. The elemental composition is presented in Table 1.

The analytical-grade chemical reagents employed included anhydrous ethanol, acetone, isopropanol, nickel

**Table 2.** Electrodeposition parameters of process 1.

Parameter	Value
Nickel Chloride Hexahydrate	200 g/L
Boric Acid	30 g/L
Potassium Chloride	30 g/L
Sodium Lauryl Ether Sulfate	0.1 g/L
Current Density	6 A/dm <sup>2</sup>
Electrode Gap	2 cm
Agitation	300 rpm
Temperature	60°C
Time	10 min

chloride, myristic acid, sodium chloride, hydrochloric acid, potassium chloride, boric acid, sodium dodecyl sulfate, and sodium bicarbonate.

### 2.2. Surface preparation

The A36 steel specimens were initially embedded in bakelite resin using hot mounting, exposing an area of 10 x 15 mm<sup>2</sup>. Subsequently, the samples underwent a sequential sanding process with grit sizes of #220, #400, #600, #800, #1000, and #1200.

Following ultrasonic cleaning in isopropanol and acetone (5 min, each), a surface activation process was conducted. This step consisted of immersing the specimens sequentially for 20 seconds in distilled water; 50 seconds in HCl (1:1 v/v); 20 seconds in distilled water; 20 seconds in NaHCO<sub>3</sub> (80g/l) and finally, 20 seconds in distilled water. The activated surfaces were then subjected to the electrodeposition process.

### 2.3. Electrodeposition process

Two electrodeposition processes were conducted for the fabrication of superhydrophobic surfaces: galvanostatic method (Process 1) and potentiostatic method (Process 2).

In electrodeposition, the potentiostatic and galvanostatic methods differ in how they control electrical potential or current during the process. Potentiostatic maintains constant potential, while galvanostatic maintains constant current<sup>8,9</sup>. The former is suitable for precise control of deposit quality and material structure, while the latter is preferable for fast and uniform deposition, especially in mass production. Potentiostatic method provides control over deposit crystalline structure and composition, advantageous in applications where precise composition is crucial<sup>8,12</sup>. On the other hand, galvanostatic method is preferable when deposition speed is paramount or deposit composition is not critical, such as in protective coatings<sup>9,10,12</sup>.

Process 1 employed an electrolytic solution formulated in aqueous medium. The specific concentration of reagents and electrodeposition parameters of Process 1 are detailed in Table 2. The electrodeposition parameters listed were chosen based on previous studies that successfully produced a uniform nickel coating on steel substrate<sup>7,9,12</sup>.

Due to the insolubility of myristic acid in water, an ethanolic solution was employed in Process 2. Table 3 presents the concentration of reagents and electrodeposition parameters used in the potentiodynamic process. The listed electrodeposition parameters were chosen based on a previous study that successfully produced a superhydrophobic coating based on nickel and myristic acid<sup>8</sup>.

## 2.4. Samples identification

Three different coatings conditions were achieved: pure nickel (E10), nickel associated with myristic acid (E01); and a bilayer structure consisting of a base layer of pure nickel succeeded by an additional layer of nickel enriched with myristic acid (E11). The uncoated specimens were labeled as E00. Pure nickel was obtained through electrodeposition using process 1, and the layer of nickel associated with myristic acid was obtained through process 2. Therefore, E11 samples underwent a sequence of both processes to obtain the bilayer coating.

## 2.5. Surfaces characterization

### 2.5.1. Analysis of morphology and chemical composition

The morphological analysis of the coatings was conducted using Scanning Electron Microscopy (SEM) with a Tescan Mira3 Scanning Electron Microscope, operating at a 15 mm working distance and 15 kV voltage. Image acquisitions were facilitated by the MiraTC software.

The chemical composition of the surfaces was carried out using Energy-Dispersive X-ray Spectroscopy (EDS) coupled to SEM, employing an Oxford Xact model, with spectra acquired through the AZtec software.

To identify the deposition of the surface energy reducing agent, the analysis of organic groups present in the samples was performed using Fourier Transform Infrared Spectroscopy (FTIR) with a Jasco FT/IR 4600 spectrophotometer.

The crystalline structure and preferred orientation of the obtained coatings were determined using X-ray diffraction analysis (XDR) employing SHIMADZU XRD-7000 Diffractometer (Cu-K $\alpha$  radiation)

### 2.5.2. Evaluation of surface wettability

To assess the wettability of the investigated surfaces and identify the superhydrophobic property, contact angle (CA) measurements were conducted using an Biolin Scientific Attension optical tensiometer. The images were captured and analyzed with the OneAttension 3.0 software. The CA results were determined by averaging three measurements obtained from 10  $\mu$ m water droplets dispensed onto the surface using an automatic pipette.

**Table 3.** Electrodeposition parameters of process 2.

Parameter	Value
Nickel Chloride Hexahydrate	200 g/L
Myristic Acid	22.8 g/L
Voltage	30V
Electrode Gap	2 cm
Time	10 min

### 2.5.3. Analysis of anticorrosive properties

To assess the corrosion resistance potentiodynamic linear polarization tests and electrochemical impedance spectroscopy (EIS) were performed using a three-electrode electrochemical cell. The specimens under investigation functioned as the working electrode, while a platinum electrode and a saturated calomel electrode (SCE) served as the counter and reference electrodes, respectively. The electrolyte used was a 3.5% w/v aqueous solution of NaCl.

The tests were initiated from the open circuit potential (OCP) after 24 hours to ensure system stabilization. For the EIS test, a frequency range of 100 kHz to 10 mHz and an amplitude of 10 mV were established. The polarization test involved measurements ranging from +0,5 V to -0,5 V relative to the OCP of 24 hours, with a scan rate of 10 mV/s. These experiments were conducted using the AUTOLAB GALVANOSTAT potentiostat, interfaced with a computer and controlled by the NOVA 2.0 program.

To assess the corrosion morphology, optical micrographs of the surfaces were obtained before and after electrochemical tests. A Zeiss Axio Zoom V16 optical microscope was used, operating with the AxioVision software.

## 3. Results and Discussion

### 3.1. Analysis of morphology and chemical composition

The SEM micrographs in Figure 1 depict the surface morphology of the various coatings obtained. The uncoated sample (E00), shown in Figure 1a, presents parallel lines indicative of the grinding process. On the other hand, the E10 (Figure 1b), E01 (Figure 1c) and E11 (Figure 1d) specimens exhibited noticeable surface modifications compared to E00, suggesting the successful incorporation of deposits on all three surfaces. These modifications resulted in variations of morphology, porosity and refinement of deposited crystals.

The nickel coating applied in condition E10, depicted in Figure 1b, exhibited enhanced homogeneity and compactness, with no exposed substrate areas. The formation of refined crystals with an acicular morphology was evident. E01 and E11 surfaces (Figures 1c and d, respectively) showcase clusters displaying a morphology reminiscent of cauliflower, a phenomenon also corroborated in research involving nickel coatings associated with the potentiostatic deposition method in an alcoholic medium in conjunction with surface energy-reducing agents obtained via electrodeposition<sup>8,37-41</sup>.

Upon analyzing and comparing conditions E01 and E11, it is evident that the doubly coated surface displayed a more voluminous coating with larger cauliflower-like clusters. According to Xiang et al.<sup>35</sup> and Yang et al.<sup>37</sup>, this behavior can be attributed to the presence of a prior nickel layer obtained through the galvanostatic method. This layer may have created preferential deposition sites for the subsequent layer, owing to the higher electrical conductivity of nickel compared to the steel substrate, resulting in the formation of more voluminous structures.

The galvanostatic process, conducted for the E10 electrodeposition without the inclusion of myristic acid, fostered a more uniform reduction of nickel across

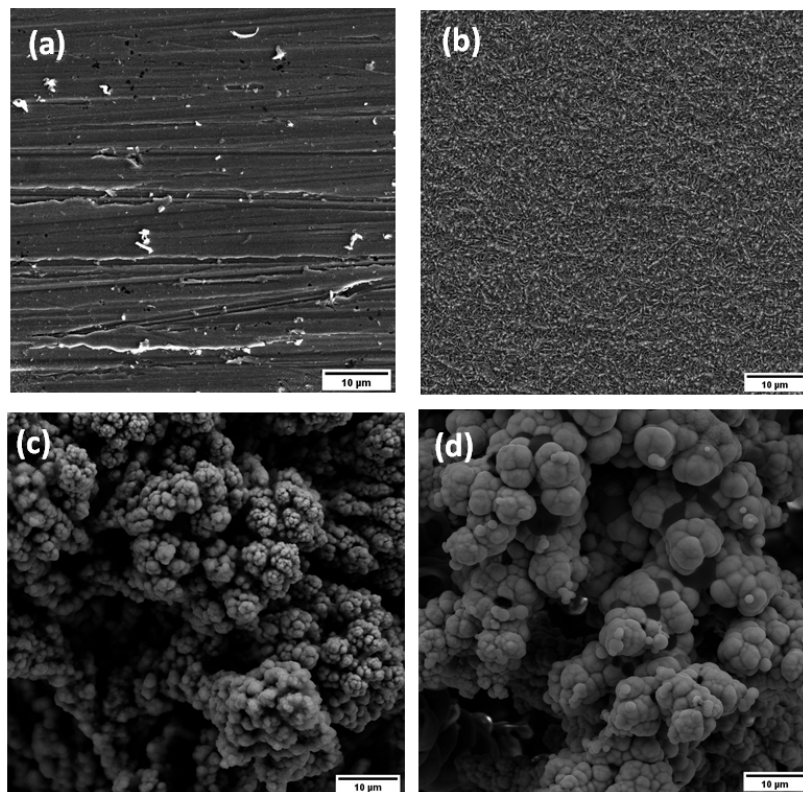


**Figure 1.** SEM images of specimens: a) E00, b) E10, c) E01 and d) E11.

the entire substrate. This behavior can be attributed to the heightened ionic mobility of cationic species in Process 1<sup>7,42</sup>, in contrast to Process 2, establishing conducive conditions for the formation of smaller nickel crystals on the surface<sup>10,43</sup>.

According to Chen et al.<sup>8</sup>, the presence of myristic acid in the electrolytic medium reduces the ionic mobility of nickel in the solution. This is attributed to the long chain of myristic acid, which imparts a more nonpolar character. Consequently, these molecules, to reach the substrate surface, need to be transported through the ionic cloud formed by nickel ions diffusing in the alcoholic solution. This effect delays the nickel reduction process on the substrate surface, leading to the formation of heterogeneous deposition regions along the surface.

The Figure 2 presents EDS diagrams of specimens and the Table 4 presents the elemental composition as a percentage for both the substrate and various coating conditions, determined through EDS analysis.

The presence of Fe and C elements in the E00 sample is consistent with the main constituents of the investigated steel (Table 1). The E10 coated surface showed the presence of Ni and O elements, confirming the successful coating deposition on the steel substrate, as evidenced by the absence of the Fe element. This aligns with the SEM results in Figure 1b, which indicated the presence of a more compact coating with no substrate exposure.

For the E01 sample, the elements Ni, O, C, and Fe were identified. The presence of nickel confirmed the coating incorporation. The elements O and C are qualitative indicators that the surface energy-reducing agent was possibly incorporated

into the coating. However, the presence of the primary element Fe of the substrate, indicates that the coating in this condition has defects and/or high porosity, allowing portions of the substrate to be exposed. This result is consistent with the micrograph previously presented for this condition in Figure 1c, where the formation of a porous coating was observed.

The E11 sample indicated the presence of Ni, C, and O elements but did not show Fe. Despite this coating also being porous, as shown in Figure 1d, the previous deposition of Ni prevented substrate exposure. The increase in the percentage of C for the E01 and E11 conditions, compared to the uncoated metal (E00), may be associated with the incorporation of myristic acid into the coatings<sup>37,38,41,43</sup>.

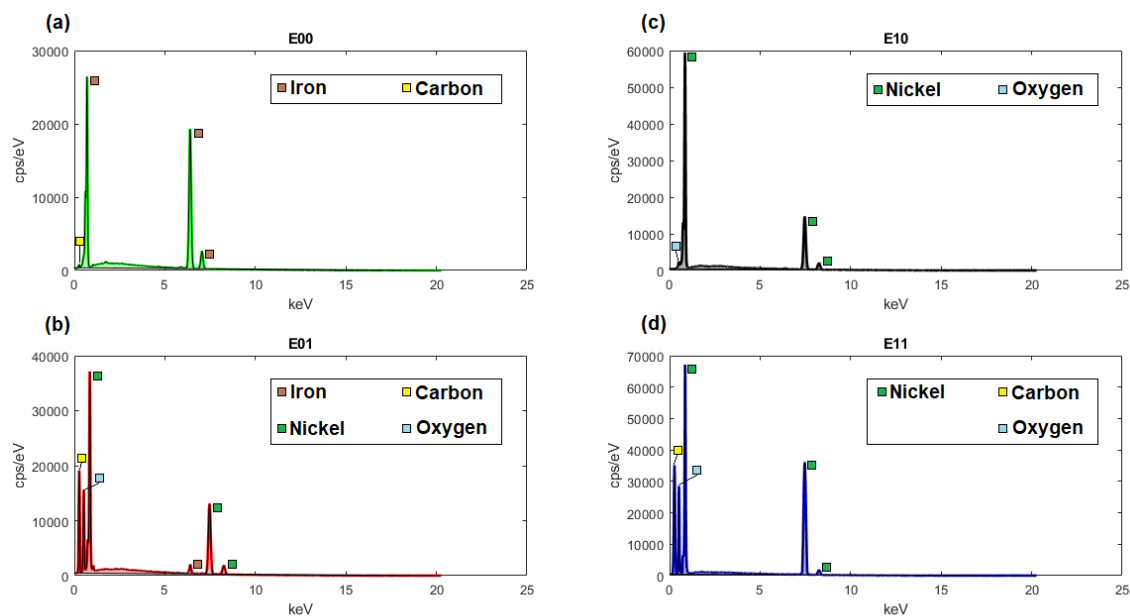
For the analysis of preferential crystallographic planes, XRD analyses were conducted. The diffractograms for both the substrate and coated samples are presented in Figure 3.

In the E00 condition, peaks near  $44,6^\circ$  and  $65,0^\circ$  were observed, corresponding to the (110) and (200) planes of Iron in the cubic system (JCPDS file card #65-4899)<sup>44-46</sup>. For the three coated samples (E10, E01, and E11), three peaks near  $44,4^\circ$ ,  $52,5^\circ$ , and  $77,0^\circ$  were identified, characteristic of the (111), (200), and (220) planes of Nickel in the cubic system (JCPDS file card #04-0850)<sup>47</sup>. The presence of Fe-related peaks observed in the uncoated sample (E00) was also identified in the E01 sample, indicating once again that the coating in this condition exhibited flaws, resulting in substrate exposure.

In order to confirm the incorporation of the surface energy-reducing agent into the coating, FTIR analysis

**Table 4.** Elemental composition of the specimens (wt%).

Sample	Elemental Composition (wt%)			
	Fe	C	Ni	O
E00	97.67	2.33	0	0
E10	0	0	98.94	1.06
E01	2.88	24.38	65.62	7.11
E11	0	14.89	80.58	4.52


**Figure 2.** EDS diagrams of specimens: a) E00, b) E10, c) E01 and d) E11.

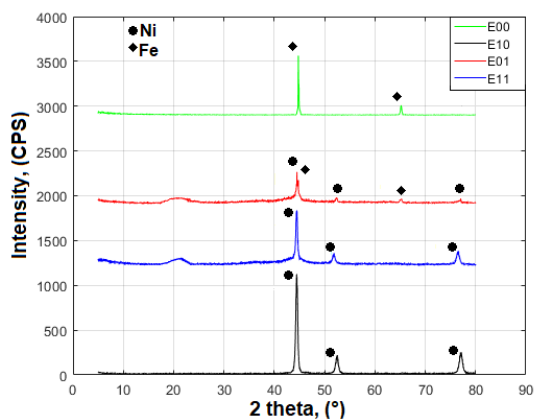
was conducted on samples E01 and E11, with the results presented in Figure 4.

In the high-frequency region, an absorption peak at  $2954\text{ cm}^{-1}$  was observed, corresponding to the asymmetric vibration of the  $-\text{CH}_3$  group<sup>6</sup>. The peaks at  $2920\text{ cm}^{-1}$  and  $2850\text{ cm}^{-1}$  are associated with the symmetric and asymmetric stretching vibrations of the  $-\text{CH}_2$  groups<sup>8,37,40</sup>. In the low-frequency region, the peaks at  $1409\text{ cm}^{-1}$  and  $1545\text{ cm}^{-1}$  correspond to the symmetric and asymmetric stretching vibrations of the organic group ( $\text{O}=\text{C}=\text{O}$ )<sup>37</sup>. The presence of  $-\text{CH}_2$ ,  $-\text{CH}_3$ , and  $\text{O}=\text{C}=\text{O}$  groups indicates the incorporation of myristic acid into the coatings. Similar findings were reported in studies conducted by<sup>37,40,41</sup>.

The results from EDS, XRD, and FTIR analyses indicated the presence of nickel and organic groups ( $\text{CH}_2$ ,  $\text{CH}_3$ , and  $\text{O}=\text{C}=\text{O}$ ) in the E01 and E11 coatings composition. Therefore, it is expected that the coating includes nickel myristate ( $\text{Ni}[\text{CH}_3(\text{CH}_2)_{12}\text{COO}]_2$ ), an ionic compound with low surface energy<sup>8,37</sup>.

### 3.2. Coating formation mechanism

The mechanism behind the formation of cauliflower-like clusters observed in samples E01 and E11 (Figure 1c, d), initiates with the application of DC voltage between the

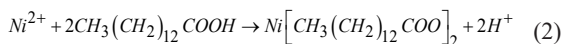

**Figure 3.** XRD patterns of the samples E00, E10, E01 and E11.

two electrodes used in the electrodeposition process (EDP), as depicted in Figure 5. In this stage, an electric field is created between the electrodes. Simultaneously, as a result of the ionic dissociation of the constituents of electrolyte,  $\text{H}^+$ ,  $\text{CH}_3(\text{CH}_2)_{12}\text{COO}^-$ ,  $\text{Ni}^{2+}$ , and  $\text{Cl}^-$  ions are dispersed in the solution<sup>37,41</sup>. Due to the presence of the electric field, the

nickel ions are more easily accelerated towards the cathodic substrate. In this cathodic region, the metal cations rapidly receive the electrons and are reduced to metallic nickel. Specific sites of metallic nickel agglomeration are then formed on the cathodic surface. These agglomerates act as the foundation for the cauliflower-like cluster formation<sup>8,38</sup>.

While the described phenomena are unfolding, additional nickel ions react with the anions provided by the dissociation of myristic acid, forming nickel myristate<sup>8,37</sup>. This ionic compound is also accelerated by the electric field and adheres to the cathodic surface, preferably in regions where the nickel clusters formed immediately before are located<sup>40</sup>. This process results in a coating that exhibits micro-nanometric structures with the presence of methylated components (CH<sub>2</sub> and CH<sub>3</sub>), which are low surface energy functional groups on the cathodic surface<sup>38,40,41</sup>.

According to Yang et al.<sup>37</sup>, the formation of nickel myristate results from the reaction between nickel ions and myristic acid, elucidated through Equations 1, 2, and 3 below:



The hydrogen ions H<sup>+</sup>, located near the cathodic substrate, also receive electrons, undergoing reduction to form molecular hydrogen during the EDP<sup>40,41</sup> process. The released H<sub>2</sub> gas contributes to the formation of a coating featuring cavities that intercalate with nickel myristate clusters, resulting in a coating that combines elevated clusters, housing low-surface-energy functional groups, and a substantial presence of small cavities<sup>36</sup>. This morphology promoted the entrapment of numerous air pockets between the treated surface and water droplets placed upon it, thereby resulting in excellent superhydrophobic performance<sup>8,37</sup>.

### 3.3. Wettability behavior

The wettability behavior of the electrodeposited coatings was examined by CA measurements. Figure 6 displays photographs of the various surface conditions investigated, along with assay details conducted on a goniometer, providing the values of the obtained CA and their corresponding standard deviations.

Sample E00 displayed hydrophilic behavior (Figure 6a), with a more extensive spreading of the water droplet observed on the substrate surface, resulting in a CA of  $51,31^{\circ} \pm 7,45^{\circ}$ . The sample coated only with Ni, E10, exhibited hydrophobic behavior, with a contact angle of  $113,85^{\circ} \pm 2,45^{\circ}$  (Figure 6b). Samples E01 (Figure 6c) and E11 (Figure 6d), which incorporated myristic acid in the electrolytic bath, displayed superhydrophobic behavior, with reduced spreading of the droplet on the coatings and a CA greater than  $150^{\circ}$ . However, the doubly coated sample, condition E11, exhibited a higher contact angle value ( $165,51^{\circ} \pm 1,02^{\circ}$ ).

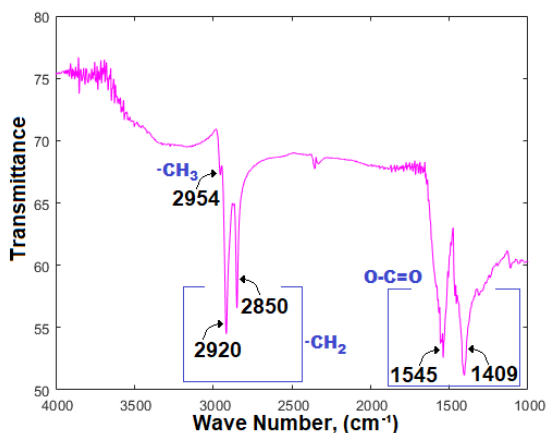


Figure 4. FTIR spectra of E01 and E11 samples.

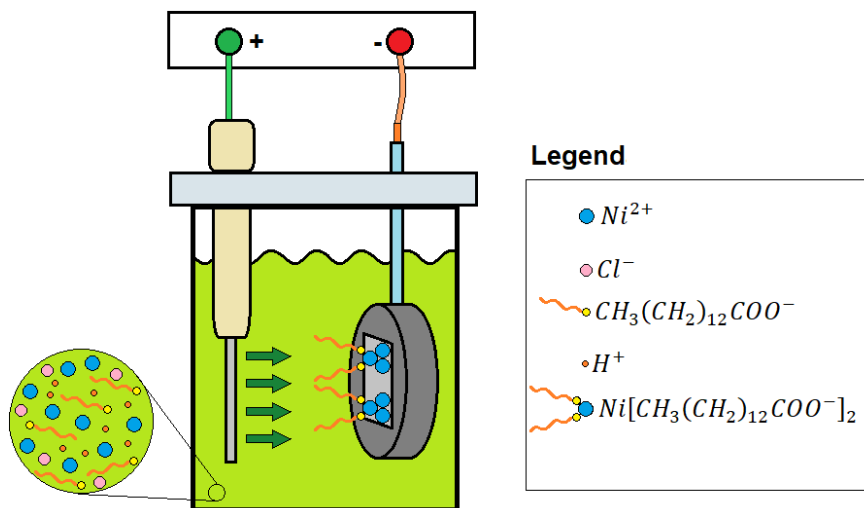
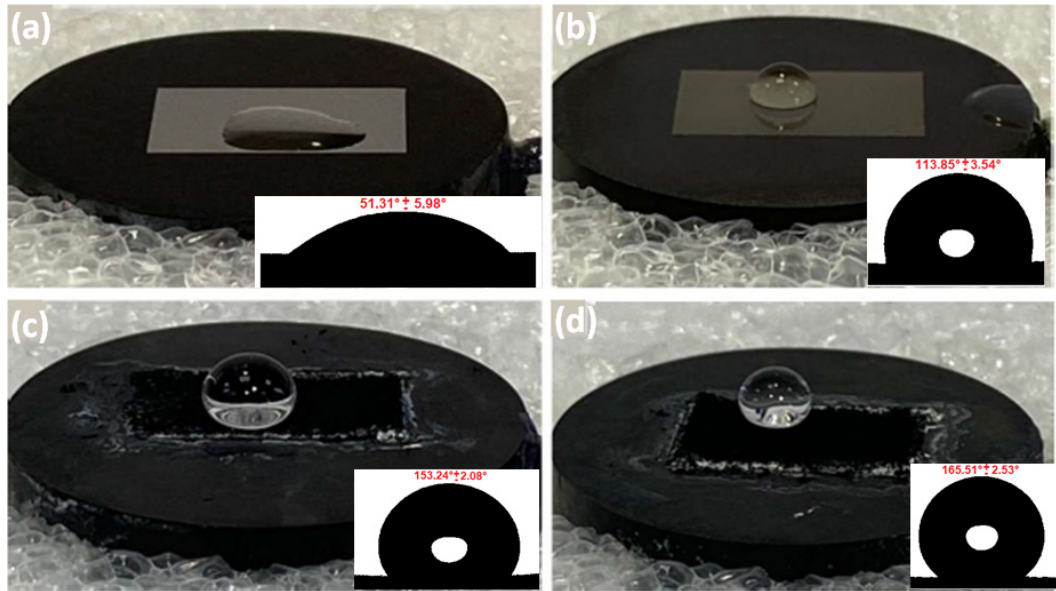


Figure 5. Nickel electrodeposited coating formation mechanism in E01 and E11.



**Figure 6.** Wettability behavior of: (a) E00, (b) E10, (c) E01, and (d) E11.

The achievement of superhydrophobic surfaces is generally associated with the formation of micro-nanometric hierarchical structures and the addition of surface energy reducing agents<sup>1,3,4</sup>. As the coatings displayed suitable roughness, as seen in the SEM images, it is possible to apply the Cassie-Baxter equation (Equation 4) to determine the fraction of the surface in contact with the water droplet, as follows:

$$\cos\theta_{CB} = f_1\cos\theta - f_2 \quad (4)$$

where  $f_1$  corresponds to the fractional area of the solid surface wetted by the water droplet, and  $f_2$  represents the fraction of air in contact with the water droplet; CB corresponds to the CA of the micro-nanostructured coating surface and is equivalent to the CA of the uncoated surface<sup>3</sup>. Since  $(f_1 + f_2 = 1)$ <sup>1</sup>,  $f_1$  was calculated, and the results are presented in Table 5.

The analysis of  $f_1$  and  $f_2$  results revealed that samples E01 and E11 presented surface wetting percentage of 6,59% and 1,96%, respectively. The presence of trapped air within the micro-nanometric structures contributed to a reduction in the contact area between the droplet and the solid surface<sup>1</sup>. This reduction is significant in the context of anticorrosive applications, as it can delay or prevent the formation of electrochemical cells<sup>4,24</sup>.

### 3.4. Analysis of anticorrosive properties

To evaluate corrosion resistance properties, EIS and polarization tests were conducted on both coated and uncoated samples. In Figure 7a, Nyquist diagrams are presented for each of the investigated surface conditions (E00, E10, E01, and E11). The Figure 7b and 7c illustrates, respectively, the equivalent electrical circuits and the impedance parameters of the coated substrate.

The sample E11 exhibited a larger capacitive arc. Generally, semicircles with a larger radius are associated with a better protective capacity of the coating<sup>7,9,15,48</sup>.

**Table 5.** Surface wetting percentage.

Sample	$f_1$	Surface Wetting Percentage
E10	0.3665	36.65%
E01	0.0659	6.59%
E11	0.0196	1.96%

Analyzing the Nyquist curves presented in Figure 7a, the E10 coating, manufactured by galvanostatic process, exhibits uniformity and absence of porosities, but lacks superhydrophobic characteristics. A larger capacitive arc is observed compared to E00 and smaller when compared to E01 and E10. In this case, the absence of superhydrophobic characteristics limits its effectiveness in corrosion protection.

The E01 coating, produced by potentiostatic process, contains a mixture of nickel with nickel myristate, conferring superhydrophobic characteristics. However, its high porosity compromises its effectiveness in corrosion protection. This is evidenced by the Nyquist plots, where the arc presented by E01 is smaller than that of E11.

The E11 coating, resulting from applying the process used in E10 followed by the process applied in E01, combines the advantages of these two samples. E11 maintains the uniformity and absence of porosities of E10 while incorporating the superhydrophobic characteristics of E01. This can be observed in the Nyquist plots, where the largest arc is presented, indicating greater resistance to corrosion.

Moreover, as expected, E00 exhibited a less favorable corrosion response, evidenced by the smaller arc compared to the other samples in the Nyquist plot.

To provide a more in-depth analysis of the behavior of surfaces exposed to the corrosive environment, the equivalent electrical circuits of the uncoated and coated samples were established, as shown in Figure 7b. These circuits were utilized to model

and adjust the data dispersion obtained in the electrochemical impedance spectroscopy (EIS) test<sup>40,49</sup>. The circuit in Figure 7b-I was used to model the results related to the uncoated sample (E00), and the remaining samples were modeled by the circuit in Figure 7b-II. Each element represented in the circuits signifies an electrochemical property of the sample undergoing the corrosion process. The Figure 7c depicts the electrochemical impedance parameters. CPE<sub>dl</sub> represents the charge separation between the substrate and the solution, while CPE<sub>f</sub> represents the charge separation between the coating and the solution. R<sub>ct</sub> denotes the charge transfer resistance between the substrate and the solution, R<sub>f</sub> denotes the coating resistance, and R<sub>s</sub> denotes the solution resistance<sup>12,48,49</sup>.

The impedance values of the Constant Phase Element (CPE) were calculated using Equation 5<sup>40</sup>.

$$CPE = Y_0^{-1} \cdot (j\omega)^{-n} \quad (5)$$

where  $Y_0$  is the module of electrical admittance,  $j$  is an imaginary unit,  $\omega$  is the angular frequency, and  $n$  is the exponent of the Constant Phase Element, which can vary as follows:  $-1 \leq n \leq 1$ . The Constant Phase Element describes an ideal inductor for  $n=-1$ , an ideal resistance for  $n=0$ , and an ideal capacitor for  $n=1$ <sup>14,40</sup>.

The resistance elements mathematically model material properties impeding charge transfer<sup>48</sup>. In this case,  $R_s$  is the electrical resistance of the electrolyte,  $R_f$  is the resistance of the coating, and  $R_{ct}$  is the charge transfer resistance between the corrosive medium and the substrate<sup>14,40</sup>.

The Constant Phase Element (CPE) elements mathematically model material properties reactive to oscillations of charge movements caused by the alternating signal. In this case, CPE<sub>f</sub> is the Constant Phase Element of the coating, and CPE<sub>dl</sub> is the Constant Phase Element of the electrical double layer<sup>12,14,40</sup>.

Figure 8a represents the Bode magnitude and phase curves of sample E00. Figure 8b represents the Bode

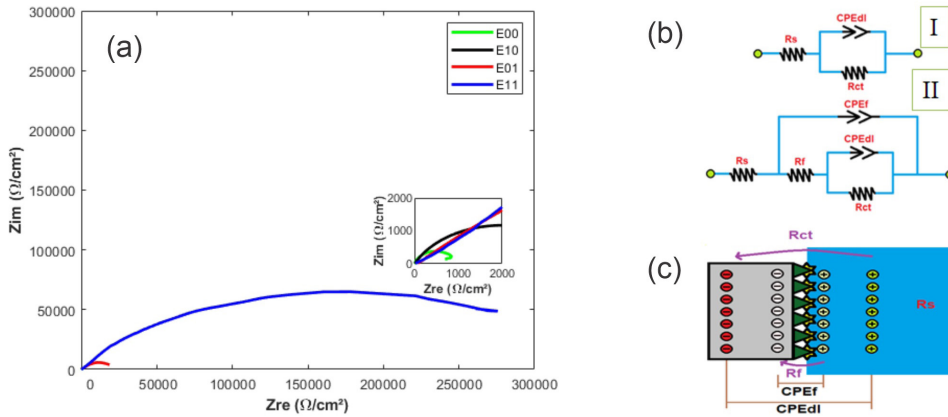


**Figure 7.** (a) Nyquist plot of investigated samples, (b) Electrical circuits modeling the corrosion process: (I) Uncoated samples, (II) Coated samples, (c) Representation scheme of impedance properties for a coated substrate.

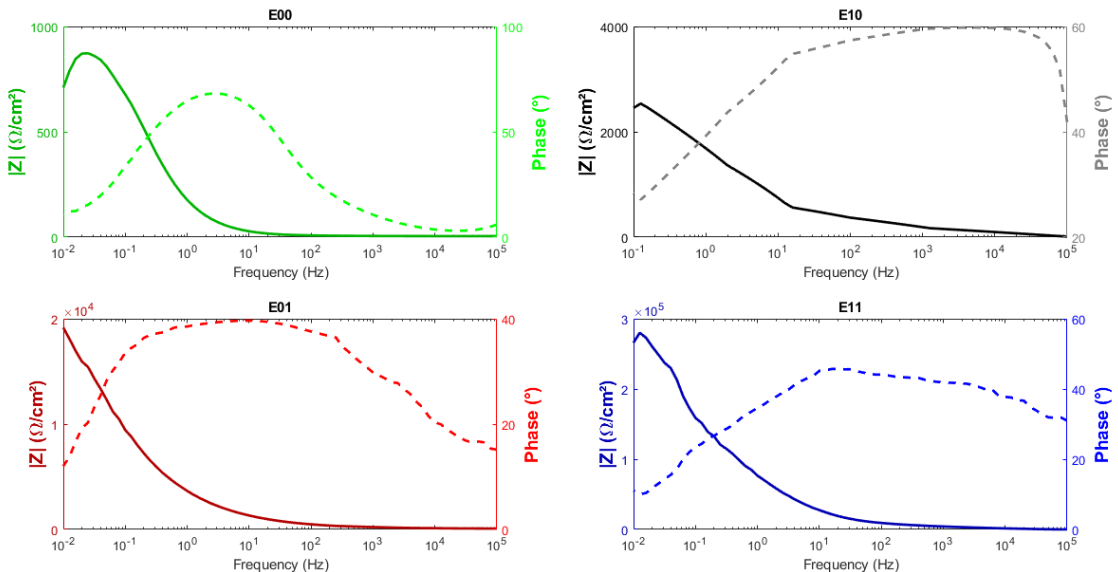


**Figure 8.** Bode plots magnitude and phase of the investigated samples: (a) E00, (b) E10, (c) E01 and (d) E11.



magnitude and phase curves of sample E10. Figure 8c represents the Bode magnitude and phase curves of sample E01. Figure 8d represents the Bode magnitude and phase curves of sample E11.

The fits shown in Figure 9 were obtained through nonlinear regression, using the least squares method, of a  $Z(f)$  function extracted from the equivalent circuit model depicted in Figure 7b-II, a procedure carried out with the aid of MATLAB. Figure 9a shows the fit of sample E10, Figure 9b shows the fit of sample E01, and Figure 9c shows the fit of sample E11. The obtained parameters are presented in Table 6.

The metric parameters:  $R^2$ , RMSE, and MAE, which are displayed in the boxes of Figures 9a, 9b, and 9c, represent respectively the coefficient of determination, Root Mean Square Error, and Mean Absolute Error of each fit.  $R^2$  varies from 0 to 1 and indicates the percentage of how well the model fits the observed data. It is noted that for all three cases,  $R^2$  was greater than 95%.

The corrosion efficiency values of the samples were calculated using Equation 6<sup>12</sup>

$$\eta\% = \left( \frac{R_{ct-coating}}{R_{ct-coating} + R_{ct-bare}} \right) \cdot 100 \quad (6)$$

An analysis of the impedance module in the low-frequency region shows that higher  $|Z|$  values were observed for sample

E11, indicating that this coating condition exhibited better protective capability<sup>40,48</sup>. It can also be observed that coating E10 had a lower  $|Z|$  value compared to conditions E11 and E01.

Analyzing the parameters presented in Table 6, it can be observed that sample E11 had the highest values for  $R_{ct}$  parameters and the lowest values for  $CPE_{dl}$ . This indicates that for this coating condition, the overall impeditive effects on the corrosion process are greater. High values of  $R_f$  and lower values of  $CPE_f$  indicate efficiency in preventing charge transfer. In this case, samples exhibiting superhydrophobic behavior (E11 and E01) showed better results for  $R_f$  and  $CPE_f$ , with E11 being the best condition.

As presented earlier in Table 5, sample E10 exhibited the highest wetting percentage in the water wetting test (36,65%), followed by sample E01 (6,59%). Sample E11 had the lowest wetting percentage (1,96%). This behavior indicates that surfaces with superhydrophobic behavior contribute to the improvement of corrosion resistance properties, as the contact of the electrolyte with the surface is reduced<sup>1,4</sup>.

The Figure 10 presents a schematic illustrating the effect of a hydrophilic surface (Figure 10a) and a superhydrophobic surface (Figure 10b) in contact with a corrosive medium (electrolyte).

Non-hydrophobic surfaces (Figure 10a) allow for greater contact with the electrolyte and, consequently, lead to a more pronounced ion exchange with the medium, resulting in a more

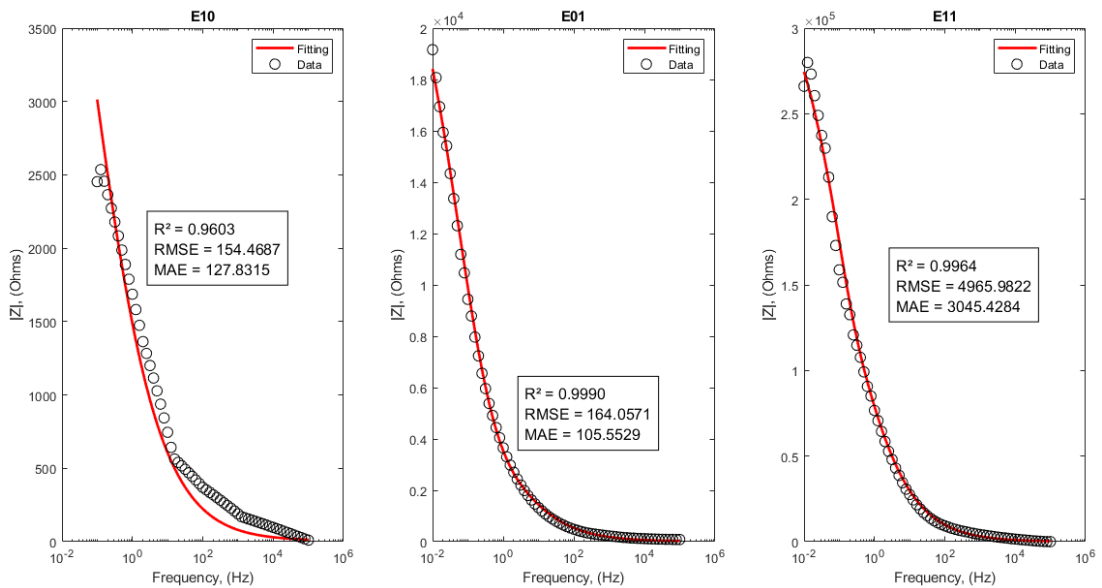


Figure 9. Fittings of impedance module curves for samples: (a) E10, (b) E01, and (c) E11.

Table 6. Electrochemical impedance parameters.

Sample	$R_{ct}$ ( $k\Omega \cdot cm^2$ )	CPEdl		$R_f$ ( $k\Omega \cdot cm^2$ )	CPEf		$R_s$ ( $\Omega \cdot cm^2$ )	$\eta\%$
		Y0	N		Y0	N		
E00	0.85	5.80.10-3	0.9107	-	-	-	6.65	0.00
E10	7.33	1.53.10-4	0.497	0.11	1.09.10-4	0.299	7.00	89.61
E01	17.50	1.46.10-4	0.900	15.21	2.29.10-4	0.478	7.85	95.37
E11	119.90	9.09.10-5	0.998	271.19	1.04.10-5	0.4939	7.65	99.30

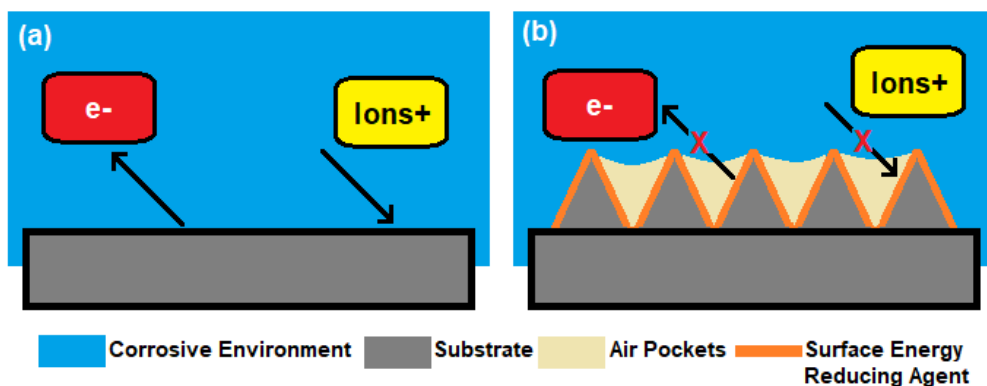


Figure 10. (a) Non-hydrophobic surface, (b) Superhydrophobic surface.

intense corrosion process<sup>4,50</sup>. In the case of superhydrophobic surfaces (Figure 10b), the presence of trapped air pockets in the micro-nanometric structures hinders the charge transfer phenomenon, minimizing or preventing the occurrence of the corrosion process<sup>13,40,41</sup>. This is the main characteristic that imparts anticorrosive properties to superhydrophobic surfaces<sup>1,26</sup>.

Besides the EIS tests, potentiodynamic polarization tests were also conducted for both coated and uncoated samples. Figure 11 displays the polarization curves, and Table 7 provides the values of potential and corrosion density for each investigated condition, obtained through the extrapolation of Tafel lines.

Potentiodynamic polarization tests provide valuable insights into the corrosion behavior of coatings. The E10 coating, manufactured via galvanostatic process, exhibits uniformity and minimal porosity, resulting in a relatively low corrosion current compared to E00 and higher than E01 and E11. However, due to the lack of superhydrophobic characteristics, its corrosion potential may not be as noble as desired, indicating moderate corrosion resistance.

In contrast, the E01 coating, fabricated through the potentiostatic process with nickel myristate, displays superhydrophobic properties but suffers from significant porosity, leading to a higher corrosion current. Despite its more noble corrosion potential compared to E10, the presence of porosities compromises its overall corrosion protection capability.

The E11 coating, a combination of processes applied to E10 followed by E01, merges the advantages of both coatings. It maintains the uniformity and low porosity of E10 while incorporating the superhydrophobic properties of E01. Consequently, E11 demonstrates a lower corrosion current and a more noble corrosion potential, indicating enhanced corrosion resistance compared to E10 and E01 individually.

Furthermore, as expected, the uncoated substrate (E00) exhibits the highest corrosion current and the least noble corrosion potential among all samples, underscoring the importance of coatings in corrosion mitigation.

From the  $E_{corr}$  and  $i_{corr}$  data (Table 7), it can be once again confirmed that the E11 coating demonstrated better corrosion protection performance, with a higher  $E_{corr}$  value (-0.2431 V) and a lower  $i_{corr}$  value ( $7.5 \times 10^{-8} \text{ A/cm}^2$ ).

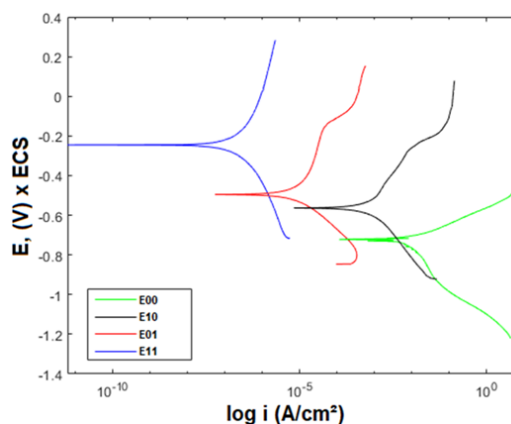


Figure 11. Linear polarization curves of sample coatings.

Table 7. Potentials currents and corrosion rates of sample surfaces.

Sample	$E_{corr}$ (V)	$i_{corr}$ ( $\text{A/cm}^2$ )
E00	-0.7257	$9.9 \cdot 10^{-3}$
E10	-0.5649	$2.5 \cdot 10^{-4}$
E01	-0.4941	$2.6 \cdot 10^{-6}$
E11	-0.2431	$7.5 \cdot 10^{-8}$

According to the literature, a low corrosion current density and a high corrosion potential value can be associated with better corrosion resistance behavior<sup>1,9,10</sup>.

Optical microscopy images were obtained to assess the changes that occurred on the surfaces of the investigated materials when exposed to a more severe corrosion test. The micrographs, before and after the polarization test, are presented in Figure 12.

As evident, the uncoated sample (E00), shown in Figure 12(a1), displayed severe corrosion, considering the inherent reactivity of ASTM A36 steel in saline environments<sup>49</sup>. Widespread surface corrosion, characterized by the generation of brown-colored corrosion products typical of iron oxides, Figure 12(a2), along with darker spots indicative of localized corrosion, was noticeable<sup>37,49</sup>.

The sample with a nickel coating (E10), obtained through a galvanostatic process without the presence of

a surface energy-reducing agent, exhibited modifications to the original coating surface, as discerned by comparing Figures 12(b1) and (b2). Localized attack, corresponding to the darker areas in the image, was observed.

The E01 coating, shown in Figure 12(c1), also displayed surface modifications, manifesting the formation of brown and orange-colored, Figure 12(c2), products typical of iron corrosion<sup>49</sup>, signifying that the electrolyte reached the substrate. Darker regions, suggesting localized corrosion, were also observed.

Polarization curves for samples E10 and E01 exhibited a segment of increased current density at higher potentials. This behavior can be associated with the process of transpassivation, where the formation of localized attacks is commonly observed<sup>4,9,14,37</sup>.

For sample E11, shown in Figure 12(d1), which exhibited better performance in the EIS test, no deposition of products associated with substrate corrosion was identified after the polarization test, and no localized attacks were observed. However, the presence of white-colored crystalline structures, Figure 12(d2), associated with the precipitation of sodium

chloride crystals, was noted<sup>13,40,47,48</sup>. Despite presenting a porous morphology on the surface, the E11 coating created an effective barrier to the electrolyte through the association of a double coating layer. The polarization curve associated with this condition showed lower current density values, and no transpassivation was observed, indicating no occurrence of localized corrosion<sup>9,12,48</sup>.

Figure 13 presents a representation of the protective mechanism for superhydrophobic behavior samples, E01 and E11, which showed different performances in electrochemical tests.

Considering the presence of surface defects in both coating conditions, as illustrated in Figure 13a, for the E01 coating, the steel substrate would be directly exposed to the corrosive environment, while for the E11 coating, the initial nickel layer would prevent direct contact of the electrolyte with the steel.

Figure 13b indicates that if these samples are immersed in a corrosive environment, the liquid will fill the space left by the coating failure point, and charge transfer will occur more pronouncedly<sup>1,9,12,51</sup>. In this case, the E01 sample is

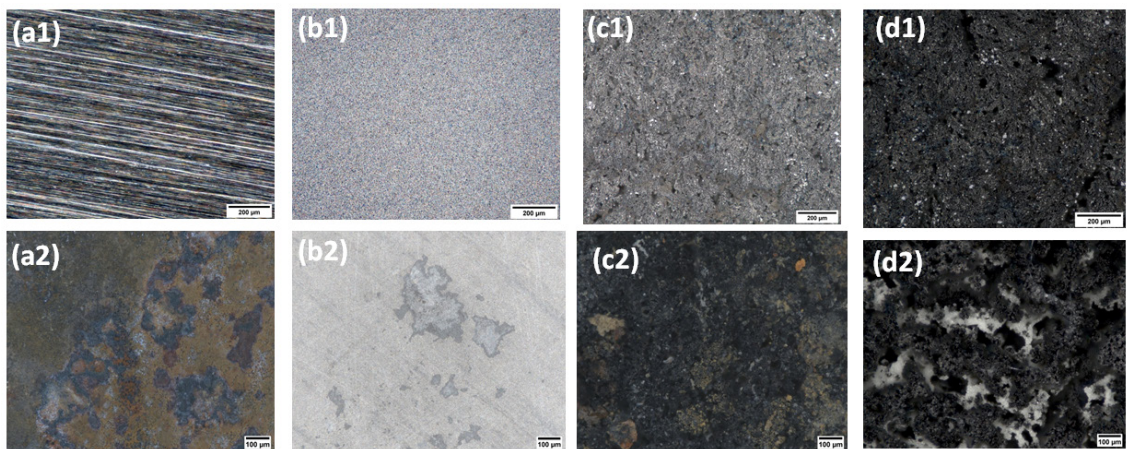


Figure 12. Optical micrographs of the surfaces: (a) E00; (b) E10; (c) E01; (d) E11; with (1) before and (2) after electrochemical tests.

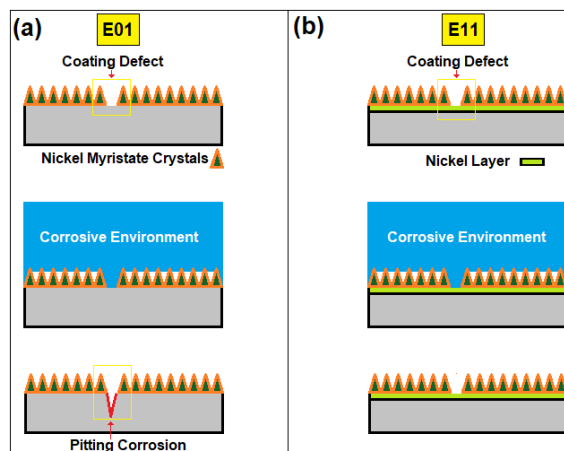


Figure 13. Representation of the mechanism of protection for coatings: (a) E01; (b) E11.

more affected, as in the regions of coating failure, a galvanic cell with an extensive cathodic area (nickel/nickel myristate) and a small anodic area (steel) will form, favoring pit propagation due to the more noble electrochemical nature of nickel compared to iron<sup>12,15,37</sup>. In the E11 sample, with no exposed steel areas, there is no formation of galvanic cells, which is one of the reasons why localized corrosion was not identified after the polarization test for this condition.

## 4. Conclusions

In summary, a deposited super-hydrophobic nickel coating on ABNT A36 steel substrate was successfully prepared by the electrodeposition technique, and its improvement of corrosion resistance was also investigated. It were obtained contact angle value of 165,51° to the E11 condition (double coating).

The SEM images indicated that the steel surface became much rough withpacked hierarchical micro/nanoscale cauliflower like clusters after the deposition of nickel film associated to miryctic acid. Such surface texture can contribute to trapping large amount of air, that would prevent the water droplet from penetrating into the steel surface, showing a super-hydrophobic property.

The results of surface chemical compositions confirm that the super-hydrophobic surfaces were comprised of nickel crystals (Ni) and nickel myristate crystals (Ni[CH<sub>2</sub>(CH<sub>2</sub>)<sub>12</sub>COO]<sub>2</sub>). FT-IR spectrum further confirm that the nonpolar functional groups of (–CH<sub>3</sub> and –CH<sub>2</sub>) were attached on the coating, which can lower the surface free energy and contribute to super-hydrophobicity of electrodeposit.

The formation mechanism of the electrodeposited super-hydrophobic coating was schematically illustrated. Compared with the uncoating steel the fabricated super-hydrophobic surface behaved better corrosion resistance, which can be proved by the potentiodynamic polarization tests and EIS measurements, and microscopic analyse after eletrochemical tests . The deposition of a preliminary layer of pure nickel, followed by a second layer of nickel and nickel myristate crystals promoted a better anti-corrosion protection mechanism, preventing the formation of pits corrosion.

Based on the results of potentiodynamic polarization tests and electrochemical impedance spectroscopy, it can be concluded that the E11 coating, obtained by combining the processes applied to E10 and E01, exhibits the best corrosion resistance. While the E10 coating shows uniformity and low porosity, its lack of superhydrophobic characteristics limits its effectiveness. On the other hand, the E01 coating, despite its superhydrophobic properties, is compromised by high porosity. E11 overcomes these limitations by combining the uniformity of E10 with the superhydrophobic properties of E01, resulting in superior corrosion resistance.

In this study, the corrosion performance was consistent with surface wettability, because the super-hydrophobic surface can prevent the corrosive ions (Cl<sup>-</sup>) to contact the bare metal surface.

Using the electrodeposition process, a simple and fast method was developed to obtain super-hydrophobic coatings with high anti-corrosion protection performance for steel surfaces. The study is relevant and promising for industrial application, given the large and constant use of steel in the most diverse sectors, as well as its high susceptibility to corrosion in saline environments.

## 5. Acknowledgments

This research was performed at the Federal University of Pernambuco/Brazil by the National Institute of Technology in Union and Materials Coating (INTM), Laboratory of Composite Materials and Structural Integrity (LBC-Compolab) and Research Institute in Petroleum and Energy (LITPEG). This work has been supported by the National Council of Scientific and Technological Development (CNPq/Brazil) (n° 409725/2023-4); Folks Improvement Coordination of Higher Education (CAPES); Financier of Studies and Projects (Finep); National Agency for Petroleum, Natural Gas and Biofuels (ANP) and Support Foundation for Science (FACEPE).

## 6. References

- Liu J, Fang X, Zhu C, Xing X, Cui G, Li Z. Fabrication of superhydrophobic coatings for corrosion protection by electrodeposition: a comprehensive review. *Colloids Surf A Physicochem Eng Asp.* 2020;607:125498.
- Darmanin T, Guittard F. Superhydrophobic and superoleophobic properties in nature. *Mater Today.* 2015;18(5):273-85.
- Wu Y, Du J, Liu G, Ma D, Jia F, Klemeš JJ, et al. A review of self-cleaning technology to reduce dust and ice accumulation in photovoltaic power generation using superhydrophobic coating. *Renew Energy.* 2022;185:1034-61.
- Mohamed AM, Abdullah AM, Younan NA. Corrosion behavior of superhydrophobic surfaces: A review. *Arab J Chem.* 2015;8(6):749-65.
- Wagner T, Neinhuis C, Barthlott W. Wettability and contaminability of insect wings as a function of their surface sculptures. *Acta Zool.* 1996;77(3):213-25.
- Bush J, Hu D, Prakash M. The integument of water-walking arthropods: form and function. *Adv Insect Physiol.* 2007;34:117-92.
- Rahimi E, Rafsanjani-Abbasi A, Kiani-Rashid A, Jafari H, Davoodi A. Morphology modification of electrodeposited superhydrophobic nickel coating for enhanced corrosion performance studied y AFM, SEM--EDS and electrochemical measurements. *Colloids Surf A Physicochem Eng Asp.* 2018;547:81-94.
- Chen Z, Hao L, Chen A, Song Q, Chen C. A rapid one-step process for fabrication of superhydrophobic surface by electrodeposition method. *Electrochim Acta.* 2012;59:168-71.
- Khorsand S, Raeissi K, Ashrafizadeh F. Corrosion resistance and long-term durability of super-hydrophobic nickel film prepared by electrodeposition process. *Appl Surf Sci.* 2014;305:498-505.
- Salehikahrizsangi P, Raeissi K, Karimzadeh F, Calabrese L, Patane S, Proverbio E. Erosion-corrosion behavior of highly hydrophobic hierarchical nickel coatings. *Colloids Surf A Physicochem Eng Asp.* 2018;558:446-54.
- Nezhad AHN, Arefinia R, Kashefi M, Davoodi A, Hosseinpour S. Compatibility of fabrication of superhydrophobic surfaces and addition of inhibitors in designing corrosion prevention strategies for electrodeposited nickel in saline solutions. *Appl Surf Sci.* 2019;493:1243-54.
- Tam J, Palumbo G, Erb U. Recent advances in superhydrophobic electrodeposits. *Materials.* 2016;9(3):151.
- Malta MIC, Vieira MRS, Silva RGC, Silva LMC, Araújo EG, Maciel SHDO, et al. Superhydrophobic surfaces on 5052 aluminum alloy obtained from LDH film modified with stearic acid for enhanced corrosion protection. *Mater Res.* 2019;22(6):e20180882.
- Liravi M, Pakzad H, Moosavi A, Nouri-Borujerdi A. A comprehensive review on recent advances in superhydrophobic surfaces and their applications for drag reduction. *Prog Org Coat.* 2020;140:105537.

15. Jena G, Thinaharan C, George R, Philip J. Robust nickel-reduced graphene oxide-myristic acid superhydrophobic coating on carbon steel using electrochemical codeposition and its corrosion resistance. *Surf Coat Tech.* 2020;397:125942.
16. Heinonen S, Huttunen-Saarivirta E, Nikkanen JP, Raulio M, Priha O, Laakso J, et al. Antibacterial properties and chemical stability of superhydrophobic silver-containing surface produced by sol-gel route. *Colloids Surf A Physicochem Eng Asp.* 2014;453:149-61.
17. Khalil-Abad MS, Yazdanshenas ME. Superhydrophobic antibacterial cotton textiles. *J Colloid Interface Sci.* 2010;351(1):293-8.
18. Silva RGC, Vieira MRS, Malta MIC, Silva CH, Oliveira SH, Urtiga SL Fo. Effect of initial surface treatment on obtaining a superhydrophobic surface on 5052 aluminum alloy with enhanced anticorrosion properties. *Surf Coat Tech.* 2019;369:311-22.
19. Hooda A, Goyat M, Pandey JK, Kumar A, Gupta R. A review on fundamentals, constraints and fabrication techniques of superhydrophobic coatings. *Prog Org Coat.* 2020;142:105557.
20. Ruzi M, Celik N, Onses MS. Superhydrophobic coatings for food packaging applications: a review. *Food Packag Shelf Life.* 2022;32:100823.
21. Crick CR, Gibbins JA, Parkin IP. Superhydrophobic polymer-coated copper-mesh; membranes for highly efficient oil-water separation. *J Mater Chem A Mater Energy Sustain.* 2013;1(19):5943-8.
22. Li K, Zeng X, Li H, Lai X. Facile fabrication of a robust superhydrophobic/superoleophilic sponge for selective oil absorption from oily water. *RSC Adv.* 2014;4:23861-8.
23. Bai Z, Zhang B. Fabrication of superhydrophobic reduced-graphene oxide/nickel coating with mechanical durability, self-cleaning and anticorrosion performance. *Nano Materials Science.* 2020;2(2):151-8.
24. Dalawai SP, Aly MAS, Latthe SS, Xing R, Sutar RS, Nagappan S, et al. Recent advances in durability of superhydrophobic self-cleaning technology: a critical review. *Prog Org Coat.* 2020;138:105381.
25. Pozzato A, Zilio S, Fois G, Vendramin D, Mistura G, Belotti M, et al. Superhydrophobic surfaces fabricated by nanoimprint lithography. *Microelectron Eng.* 2006;83(4-9):884-8.
26. Yang Y, He H, Li Y, Qiu J. Using nanoimprint lithography to create robust, buoyant, superhydrophobic PVB/SiO<sub>2</sub> coatings on wood surfaces inspired by red roses petal. *Sci Rep.* 2019;9(1):9961.
27. Acatay K, Simsek E, Ow-Yang C, Menciloglu Y. Tunable, superhydrophobically stable polymeric surfaces by electrospinning. *Angew Chem Int Ed Engl.* 2004;43:1.
28. Ma M, Mao Y, Gupta M, Gleason KK, Rutledge GC. Superhydrophobic fabrics produced by electrospinning and chemical vapor deposition. *Macromolecules.* 2005;38(23):9742-8.
29. Zhu M, Zuo W, Yu H, Yang W, Chen Y. Superhydrophobic surface directly created by electrospinning based on hydrophilic material. *J Mater Sci.* 2006;41(12):3793-7.
30. Zheng J, He A, Li J, Xu J, Han C. Studies on the controlled morphology and wettability of polystyrene surfaces by electrospinning or electrospraying. *Polymer.* 2006;47(20):7095-102.
31. Barkhudarov PM, Shah PB, Watkins EB, Doshi DA, Brinker CJ, Majewski J. Corrosion inhibition using superhydrophobic films. *Corros Sci.* 2008;50(3):897-902.
32. Cai Z, Lin J, Hong X. Transparent superhydrophobic hollow films (TSHFs) with superior thermal stability and moisture resistance. *RSC Adv.* 2018;8(1):491-8.
33. Darband GB, Aliofkhae M, Khorsand S, Sokhanvar S, Kaboli A. Science and engineering of superhydrophobic surfaces: review of corrosion resistance, chemical and mechanical stability. *Arab J Chem.* 2020;13(1):1763-802.
34. Zhao Y, Tang Y, Wang X, Lin T. Superhydrophobic cotton fabric fabricated by electrostatic assembly of silica nanoparticles and its remarkable buoyancy. *Appl Surf Sci.* 2010;256(22):6736-42.
35. Xiang T, Ding S, Li C, Zheng S, Hu W, Wang J, et al. Effect of current density on wettability and corrosion resistance of superhydrophobic nickel coating deposited on low carbon steel. *Mater Des.* 2017;114:65-72.
36. Chen Z, Zhu C, Cai M, Yi X, Li J. Growth and morphology tuning of ordered nickel nanocones routed by one-step pulse electrodeposition. *Appl Surf Sci.* 2020;508:145291.
37. Yang Z, Liu X, Tian Y. Fabrication of super-hydrophobic nickel film on copper substrate with improved corrosion inhibition by electrodeposition process. *Colloids Surf A Physicochem Eng Asp.* 2019;560:205-12.
38. Chen Z, Hao L, Chen C. A fast electrodeposition method for fabrication of lanthanum super-hydrophobic surface with hierarchical micro-nanostructures. *Colloids Surf A Physicochem Eng Asp.* 2012;401:1-7.
39. Liu Y, Yin X, Zhang J, Yu S, Han Z, Ren L. A electro-deposition process for fabrication of biomimetic super-hydrophobic surface and its corrosion resistance on magnesium alloy. *Electrochim Acta.* 2014;125:395-403.
40. Jiang S, Guo Z, Deng Y, Dong H, Li X, Liu J. Effect of pulse frequency on the one-step preparation of superhydrophobic surface by pulse electrodeposition. *Appl Surf Sci.* 2018;458:603-11.
41. Liu Q, Kang Z. One-step electrodeposition process to fabricate superhydrophobic surface with improved anticorrosion property on magnesium alloy. *Mater Lett.* 2014;137:210-3.
42. Zhu Y, Zheng H, Yang Q, Pan A, Yang Z, Qian Y. Growth of dendritic cobalt nanocrystals at room temperature. *J Cryst Growth.* 2004;260(3-4):427-34.
43. Liang SH, Yu T, Liu DP, Wang WX, Wang YP, Han XF. Characterization of stearic acid adsorption on Ni(111) surface by experimental and first-principles study approach. *J Appl Phys.* 2011;109(7):07C115.
44. Zhang J, Guyot F. Thermal equation of state of iron and Fe<sub>0.91</sub>Si<sub>0.09</sub>. *Phys Chem Miner.* 1999;26:206-11.
45. Wilburn DR, Bassett WA. Hydrostatic compression of iron and related compounds: an overview. *Am Mineral.* 1978;63:591-6.
46. Jørgensen JE, Smith RI. On the compression mechanism of FeF<sub>3</sub>. *Acta Crystallogr B.* 2006;62(6):987-92.
47. Davey WP. Precision measurements of the lattice constants of twelve common metals. *Phys Rev.* 1925;25(6):753-61.
48. Carvalho LA, Andrade AR, Bueno PR. Electrochemical impedance spectroscopy applied to the study of heterogeneous reactions in dimensionally stable anodes. *Quim Nova.* 2006;29:796-804.
49. Silva MVF, Pereira MC, Codaro EN, Acciari HA. Corrosion of carbon steel: an everyday approach in teaching chemistry. *Quim Nova.* 2015;38(2):293-6.
50. Lisboa A, Barin CS. Eletrodeposição de ligas metálicas nobres para fabricação de joias e joias folheadas. *UNOPAR Sci Exact Tech Sci.* 2009;8(1):27-33.
51. Vazirinasab E, Jafari R, Momen G. Application of superhydrophobic coatings as a corrosion barrier: a review. *Surf Coat Tech.* 2018;341:40-56.